Chapter 6

The Advanced Charge Injection Techniques Towards the Fabrication of High-Power Organic Light Emitting Diodes

Dashan Qin and Jidong Zhang

Additional information is available at the end of the chapter

http://dx.doi.org/10.5772/52446

1. Introduction

1.1. General descriptions of OLEDs

In general, an organic light emitting diode (OLED) contains a system of thin organic layers sandwiched between two electrode layers (anode and cathode). When a voltage is applied, light is generated within the system of organic layers and emerges through one of the transparent electrodes. The OLED fabricated onto a glass substrate is considered as a surface light source less than 2 millimeters (mm) thick. In contrast to conventional light sources, OLEDs emit wide-area light with high-quality color rendering, which is very pleasant for the human eye, and also needs no reflectors to reduce glare. As a result, OLEDs are one of the hottest research areas being intensely developed in the photonic industry.

The thin organic layers of an OLED can be prepared either via the vacuum deposition or solution casting, with a total thickness of approx. 200-400 nanometers (nm). If the solution casting is employed to make organic or polymeric thin films, the under layer must be free from the destruction brought by the solvent of the upper layer, therefore, solution-processed OLEDs often have only one or two organic layers. However, if the vacuum deposition is adapted to make organic small-molecule thin films, the upper layer causes no harm to the under ones. Thus, vacuum-deposited OLEDs are always multi-layered. Compared to the solution casting, the vacuum deposition enables OLEDs to have much higher injection efficiency, luminance, and lifetime.

1.2. Hole injection in OLEDs

The light emission from an electrically driven OLED occurs due to the recombination of positive and negative charge carriers, hereafter called as holes and electrons, respectively

INTECH
open science | open minds

© 2012 Qin and Zhang, licensee InTech. This is an open access chapter distributed under the terms of the Creative Commons Attribution License (http://creativecommons.org/licenses/by/3.0), which permits unrestricted use, distribution, and reproduction in any medium, provided the original work is properly cited.

[1]. The number of holes (or the hole current) is limited by the hole injection from anode to organic layer, which is controlled by the Schottky barrier height at the anode/organic interface. If pristine based organic hole transporters are used, for example, N,N'-bis-(1-naphthl)-diphenyl-1,1'-biphenyl-4,4'-diamine (NPB), 4,4′-N,N′-dicarbazole-biphenyl (CBP), 4,4′,4′′-tris(N-3-methylphenyl-N-phenylamino)triphenylamine (m-MTDATA), because the Fermi level of the high-work function anode is pinned at about 0.5-0.6 eV above the energy level of highest occupied molecular orbital (HOMO) of organic hole transporters [2, 3], the injection barrier is always no less than 0.5 eV, leading to inefficient hole injection and thereby high driving voltage in such OLEDs. However, if the p-doped materials are utilized, an efficient hole injection can be achieved. In this case, athough the barrier height of hole injection remains almost the same and unchanged by the intervention of the p-doped layer, holes can easily tunnel into organic layer of an OLED through the very thin depletion zone formed at the interface of p-doped material and anode even at very low driving voltage [4]. In this chapter, we introduce a method of efficient hole current generation at the interface of electron donor and acceptor, in clear contrast to the above-mentioned hole injection technologies, and discuss its potential applications in OLEDs [5-7].

1.3. Electron injection in inverted OLEDs

The active matrix displays based on OLEDs have been successfully applied to portable electronic devices, e.g., mobile phones and music players. In order to facilitate the large-scale commercialization for active matrix OLED displays, it is of great necessity to reduce their fabrication cost. Hence, the n-channel amorphous silicon thin-film transistor technology may preferably be utilized to drive the light emitting elements, but requires the OLED structure with inverted layer sequence [8, 9]. Compared to the regular OLEDs, higher driving voltages are always obtained in the inverted ones due to the poor electron injection as a consequence of the inefficient metal penetration into organics [10,11]. Thus, the n-doped electron transport layers (n-ETLs) are adopted to enhance the electron current in inverted OLEDs [4], e.g., lithium doped bathcuproine (BCP). However, the electron injection from the cathode into n-ETL in the inverted OLED is found always less efficient than that in the regular OLED. Thomschke et al. [12] improved the electron injection in a n-i-p OLED via inserting an interlayer of Bphen double-doped with cesium and silver between the silver cathode and cesium-doped Bphen, followed by the thermal annealing of the whole device. Though this method led to almost the same electrical properties in the inverted OLEDs as those in the regular OLEDs, it is relatively complicated and therefore unsuitable for use in the mass production of the active matrix OLED displays. Here, we introduce the increased electron injection in inverted bottom-emission OLEDs (IBOLEDs) via using the combination of two n-ETLs [13-16].

2. Experimental methods

100-nm-thick indium tin oxide (ITO) thin film coated glass substrates were commercially bought with a sheet resistance of 10-30 Ω per square, used as the anode in the conventional OLEDs and as the cathode in the inverted OLEDs. After being cleaned in acetone, alcohol,

and de-ionized water sequentially by an ultrasonic horn, the patterned ITO substrates were blown dry by nitrogen gun and then treated in UV-ozone for 15 min. The base vacuum pressures of the thin film and device fabrications were 1×10^{-5} to 4×10^{-4} Pa.

Copper phthalocyanine (CuPc, electron donor) and 3, 4, 9, 10 perylenetetracarboxylic dianhydride (PTCDA, electron acceptor) were used to form the interfaces of generating holes and electrons. Molybdenum oxide (MoO_3) and NPB were adopted as hole injection and transport materials, respectively. Tris(8-quinolinolato) aluminum (Alq3) and BCP were chosen as the emissive and electron transport materials, respectively. The lithium carbonate was selected as an n-dopant to the PTCDA and BCP. 1,4,5,8-naphthalene-tetracarboxylic-dianhydride (NTCDA) was also chosen to form an n-doped material with ITO.

The current versus voltage (I-V) characteristics of the devices were measured by a programmable Keithley 2400 sourcemeter or a Keithley electrometer 617, and the device luminance was recorded by an ST-86LA spot photometer. The optical absorption spectra of organic thin films were obtained using a Cary 300 spectrophotometer or an UV-3100 spectrophotometer. The X-ray diffraction (XRD) measurements were performed on an X-ray diffractometer (D/max-RB).

3. Results and discussion

3.1. Hole generation at the interfaces of electron donor (CuPc) and acceptor (PTCDA) in OLEDs

Pairs of organic donors and acceptors have been applied in organic solar cells to realize the efficient photo-to-electricity conversion since 1986 [17]. The underlying mechanism for organic photovoltaic devices is the photoinduced electron transfer from donor to acceptor, generating free holes in donor and electrons in acceptor. The donors and acceptors in organic photovoltaic devices constitute either planar interfaces or mixed interfaces. Recently, the planar donor/acceptor interfaces have been successfully used to realize the ambipolar transport in organic field effect transistors [18, 19]. The recent work shows that the planar and mixed interfaces of donor and acceptor can generate very efficient hole current in OLEDs [5-7].

3.1.1. The hole generation at the planar CuPc/PTCDA interface

We firstly fabricated the following light emitting devices:
Device 1: ITO/ CuPc 5 nm/ NPB 75 nm/ Alq3 60 nm/ Mg:Ag/ Ag;
Device 2: ITO/ PTCDA 10 nm/ NPB 70 nm/ Alq3 60 nm/ Mg:Ag/ Ag;
Device 3: ITO/ PTCDA 20 nm/ NPB 60 nm/ Alq3 60 nm/ Mg:Ag/ Ag;
Device 4: ITO/ PTCDA 10 nm/ CuPc 5 nm/ NPB 65 nm/ Alq3 60 nm/ Mg:Ag/ Ag;
Device 5: ITO/ PTCDA 20 nm/ CuPc 5 nm/ NPB 55 nm/ Alq3 60 nm/ Mg:Ag/ Ag;

Note that, the devices 4 and 5 are fabricated with planar PTCDA/ CuPc interfaces for hole injection.

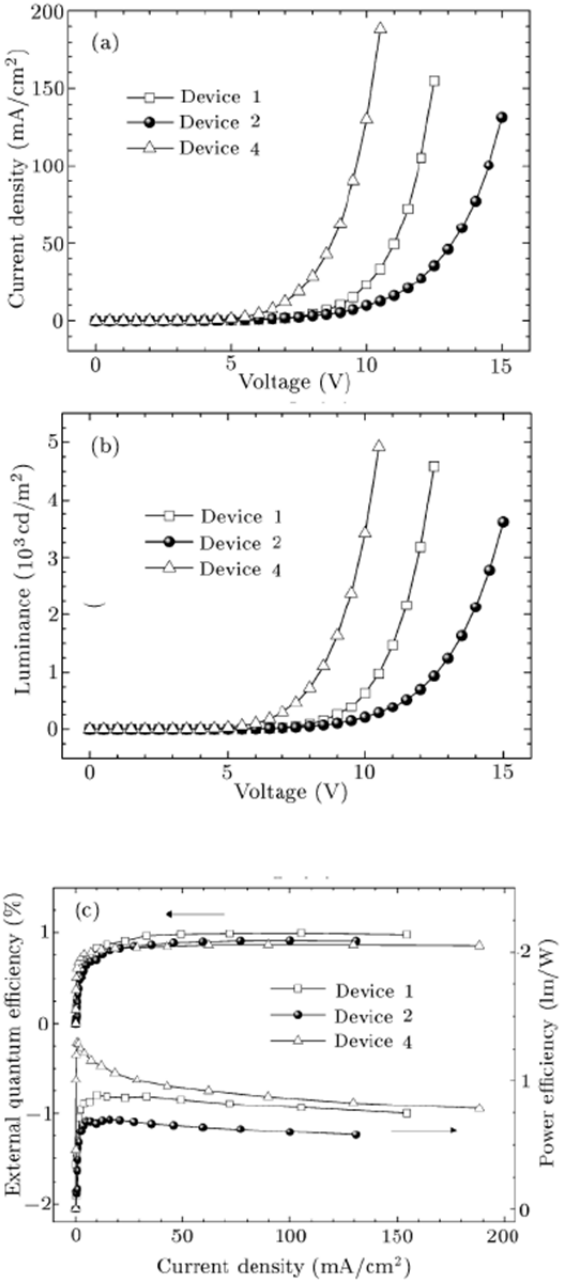

Figure 1. Characteristics of (a) I-V, (b) luminance-voltage (L-V), and (c) efficiency-current density of devices 1, 2, and 4. The external quantum efficiencies are calculated, provided that all of the devices are assumed to function as Lambertian sources.

Fig. 1 shows the properties of devices 1, 2, and 4. As shown in Fig. 1(a), device 4 reaches a current density of 130 mA/cm² at a voltage of 10 V, which is 4.6 times higher than that of 23.2 mA/cm² for device 1 and 12.3 times higher than that of 9.8 mA/cm² for device 2. There is a decrease in the operating voltage at a given current density in the order of device 2 > device 1 > device 4, clearly demonstrating the structure of ITO/ PTCDA 10 nm/ CuPc 5 nm can generate much enhanced hole current than the structures of ITO/ CuPc 5 nm and ITO/ PTCDA 10 nm. Likewise, Fig. 1(b) shows that device 4 also exhibits much higher luminance than devices 1 and 2. As seen in Fig. 1(c), there is a decrease in the external quantum efficiency (EQE) in the order of device 1 > device 2 > device 4, mostly resulting from some absorption in CuPc and PTCDA over the Alq3 emission; nevertheless, the power efficiency at a certain current density decreases in an order of device 4 > device 1 > device 2. It may thus,be concluded that the structure of ITO/ PTCDA 10 nm/ CuPc 5 nm outperforms the structures of ITO/ CuPc 5 nm and ITO/ PTCDA 10 nm in OLEDs.

In order to figure out the hole generation in OLEDs with the ITO/ PTCDA (10 and 20) nm/ CuPc structure, the influence of the PTCDA layer thickness on the device current has been studied. We have shown the observed I-V characteristics of devices 2, 3, 4 and 5 in Fig. 2. It shows that the device 2 (10 nm) has got nearly the same I-V characteristics as device 3 (20 nm), indicating that the hole generation in the ITO/ PTCDA (10 and 20) nm structure is weakly dependent on the PTCDA thickness [20], while device 4 gives much increased current density than device 5, implying that the hole generation in the ITO/ PTCDA (10 and 20) nm/ CuPc structure is strongly subject to the PTCDA layer thickness. It may therefore be concluded that besides a minor process of ITO injecting holes directly into the PTCDA layer [20, 21], devices 4 (10 nm) and 5 (20 nm) possess a major hole-generating process which devices 2 and 3 do not have.

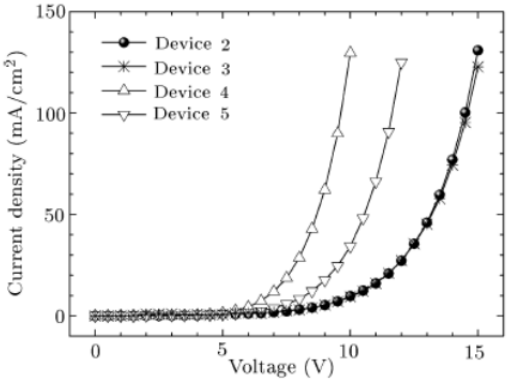

Figure 2. The I-V characteristics of devices 2 (10 nm PTCDA), 3 (20 nm PTCDA), 4 (10nm PTCDA/ CuPc) and 5 (20 nm PTCDA/ CuPc).

Fig. 3 depicts the major hole generation process in the ITO/ PTCDA (20) nm/ CuPc structure. Under the forward bias, due to the influence of holes accumulated at the ITO/ PTCDA interface [22], the PTCDA/ CuPc interface may become polarized, that is, half electrons from

the highest occupied molecular orbital (HOMO) of CuPc are transferred into the lowest unoccupied molecular orbital (LUMO) of PTCDA, which is possibly favored by the following three reasons: Firstly, the PTCDA/ CuPc interface can effectively dissociate the photo-generated excitons into hole and electrons and then prevent them from recombining [23]; secondly, there is a strong Coulomb force between PTCDA and CuPc [7], thereby making the overlap between the HOMO of CuPc and LUMO of PTCDA significant, and furthermore the electric field can assist electrons in the HOMO of CuPc overcoming 0.6 eV energy barrier to get into the LUMO of PTCDA; thirdly, the interfacial dipole at the PTCDA/ CuPc interface can facilitate the generation of hole-electron pairs [19] instead of excitons. After electrons get transferred into the LUMO of PTCDA, the vacancies (holes) are generated in the HOMO of CuPc, and those transferred into the PTCDA layer are rapidly transported into the ITO anode, generating very efficient hole current. For the ITO/ PTCDA (10 and 20) nm/ CuPc structure, when the thickness of the PTCDA layer increases, the electrostatic inducement effect of holes accumulated at the ITO/ PTCDA interface on the PTCDA/ CuPc interface, presumably considered proportional to the inverse of the square of the PTCDA layer thickness, decreases, and accordingly the charge generation at the PTCDA/ CuPc interface becomes less efficient, accounting for the decreased current density in device 3 as compared to that in device 4.

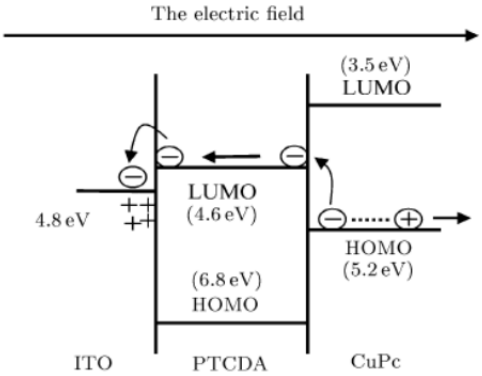

Figure 3. Schematic flat-band energy level diagram for description of the major hole-generating process in devices 4 and 5. The energy level alignments at the PTCDA/ CuPc interface have been ignored for simplicity.

3.1.2. Characterization of OLEDs with ITO/ CuPc and ITO/PTCDA:CuPc anodes

We compare the performance of two devices with structures of ITO/CuPc 5 nm/NPB 75 nm/Alq3 60 nm/Mg:Ag and ITO/PTCDA:CuPc (1:2 in mass ratio) 10 nm/NPB 70 nm/Alq3 60 nm/Mg:Ag, respectively. As shown in Fig. 4(a), the device with the ITO/ PTCDA:CuPc anode has higher current density and luminance at the same driving voltage compared to the device with the ITO/CuPc anode. In addition, as shown in Fig. 4(b), the latter has better current and power efficiencies than the device with the ITO/CuPc anode. For example, at a brightness of 2000 cd/m2, the device with the ITO/PTCDA:CuPc anode has a current

efficiency of 2.7 cd/A and a power efficiency of 1 lm/W, whereas the device with the ITO/CuPc anode has 2.3 cd/A and 0.7 lm/W, respectively. Therefore, the ITO/PTCDA:CuPc anode structure is more efficient than the ITO/CuPc anode structure.

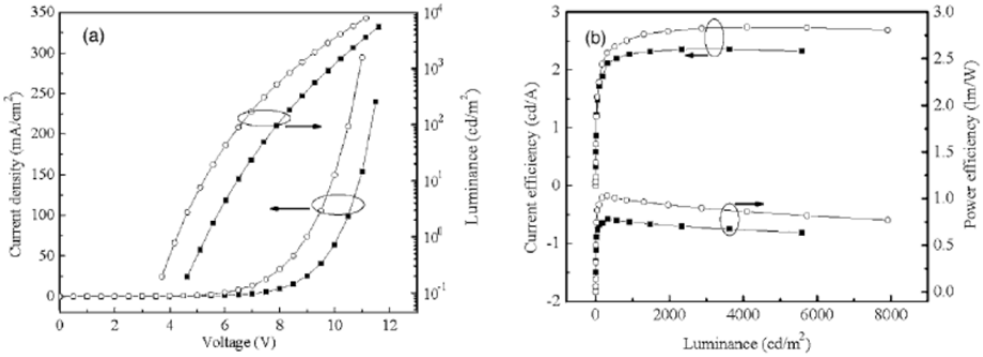

Figure 4. (a) I-V-L and (b) efficiency-luminance characteristics of two OLEDs with structures of ITO/CuPc 5 nm/NPB 75 nm/Alq3 60 nm/Mg:Ag (filled squares) and ITO/PTCDA:CuPc (1:2 in mass ratio) 10 nm/NPB 70 nm/Alq3 60 nm/Mg:Ag (open circles), respectively.

The influence of PTCDA:CuPc thickness on the device performance was studied. Fig. 5(a) shows that the maximum current efficiencies of the devices with 10 and 20 nm PTCDA:CuPc are slightly different and higher than those of the devices with 5 and 30 nm PTCDA:CuPc. The driving voltage for the devices with 10, 20, and 30 nm PTCDA:CuPc, such as at I=50 mA/cm2 or I=150 mA/cm2, is very close and all are lower than that for the device with 5 nm PTCDA:CuPc. Fig. 5(b) shows that the power efficiency of the devices with 10 and 20 nm PTCDA:CuPc is nearly the same and both are higher than those of the devices with 5 and 30 nm PTCDA:CuPc. It may therefore be concluded that the ITO/ PTCDA:CuPc anode structure is better when the thickness of PTCDA:CuPc is changed from 10 to 20 nm.

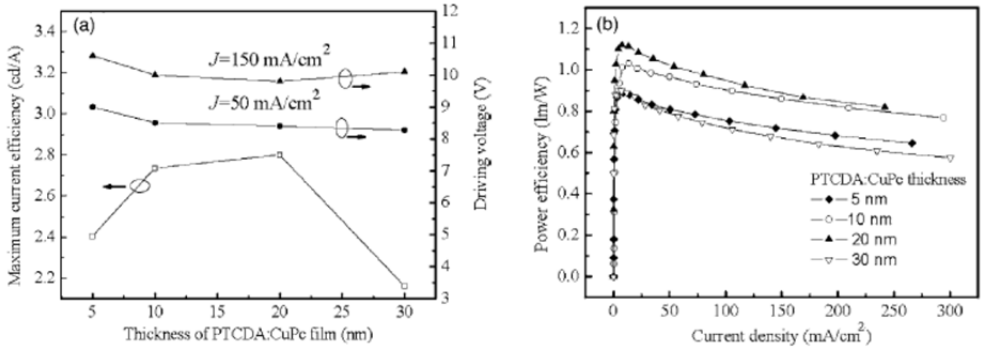

Figure 5. (a) Maximum current efficiency and driving voltage vs PTCDA:CuPc thickness and (b) plots of power efficiency as a function of current density for OLEDs with structure of ITO/1:2 PTCDA:CuPc x nm/NPB 80-x nm/Alq3 60 nm/Mg:Ag (open circles), where the PTCDA:CuPc thicknesses are 5, 10, 20, and 30 nm, respectively.

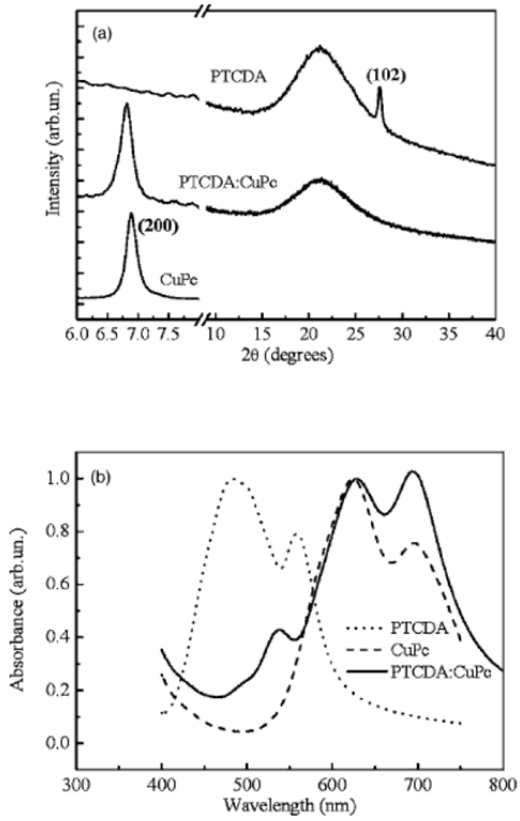

Figure 6. (a) XRD patterns and (b) absorption spectra for 100 nm CuPc, PTCDA, and 1:2 PTCDA:CuPc thin films deposited on quartz glasses.

The structural and optical properties of 1:2 PTCDA:CuPc composite have also been studied. As shown in Fig. 6(a), for the mixed PTCDA:CuPc thin film, there is a prominent peak present at $2\theta = 6.8°$, corresponding to diffraction from the (200) plane of the α-CuPc phase [18], and a broad peak present at $2\theta = 21.0°$, assigned to the reflection from the quartz substrate. This clearly demonstrates that some CuPc aggregates are crystalline, while almost all PTCDA aggregates are amorphous in the 1:2 PTCDA:CuPc film. Intermolecular hydrogen bonding is possibly formed between the outer ring of CuPc and carboxylic dianhydride of PTCDA [25]. Thus, during the codeposition, CuPc could be bonded to PTCDA and accordingly destroy PTCDA (102) aggregates, but PTCDA does not affect all of the CuPc (200) stacks, presumably ascribed to the smaller amount of PTCDA than CuPc. Fig. 6(b) displays the electronic absorption spectra of CuPc, PTCDA, and PTCDA:CuPc films. In the low-energy Q band of CuPc, as compared to CuPc film, PTCDA:CuPc film shows a decreased relative intensity of the CuPc dimeric peak at λ=629 nm to the CuPc monomeric peak at λ=693 nm, consistent with the earlier analyses of XRD data [25]. In the high-energy zone, there is a prominent absorption peak at λ=536 nm for PTCDA:CuPc film; the broad

absorption feature at λ=539 nm for neat PTCDA film [26] is strongly suppressed in PTCDA:CuPc film .

Hole generation in the ITO/PTCDA:CuPc anode cannot be simply described as holes being directly injected from ITO to PTCDA:CuPc, as the hole injection barrier from ITO to PTCDA:CuPc is not reduced, as compared to that from ITO to CuPc [5]. In order to figure out the working mechanism of the ITO/PTCDA:CuPc hole injection structure, the dependence of the device performance on NPB spacer thickness was studied. As shown in Fig. 7(a), with increasing NPB spacer thickness, the device current decreases significantly; but when the NPB spacer thickness is greater than or equal to 20 nm, the devices exhibit nearly identical I–V characteristics. Fig. 7(b) shows that the device efficiency decreases with increasing NPB spacer thickness.

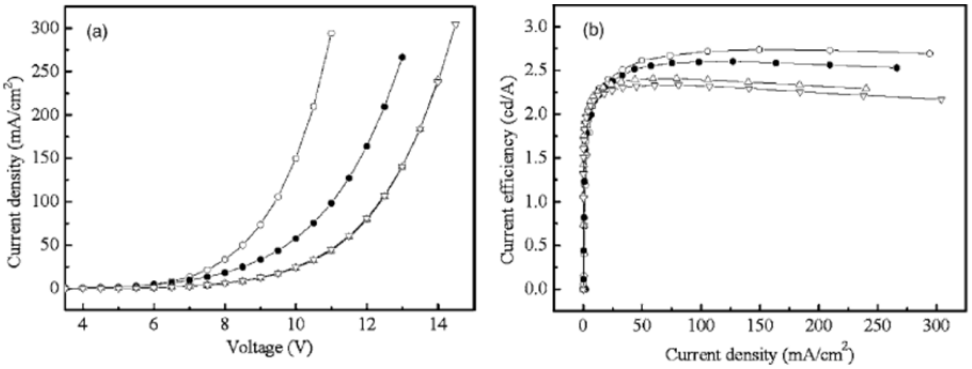

Figure 7. (a) I-V and (b) efficiency-current density curves for OLEDs with structure of ITO/ NPB spacer *x* nm/ PTCDA:CuPc 10 nm/ NPB 70-*x* nm/ Alq3 60 nm/ Mg:Ag, where NPB spacer thicknesses are 0 nm (open circles), 10 nm (filled circles), 20 nm (upward triangles), and 30 nm (downward triangles), respectively.

The variation of device current with NPB spacer thickness indicates that static-induced hole-electron pairs generation is likely to take place in PTCDA:CuPc composites, expressed as

$$\mathrm{CuPc} + \mathrm{PTCDA} \overset{\mathrm{SI}}{\rightarrow} \mathrm{CuPc}^{+} + \mathrm{PTCDA}^{-}, \quad (1)$$

where SI stands for static inducement. One paired electron in the HOMO of one CuPc molecule can be transferred to the LUMO of one PTCDA molecule in proximity, favored by (i) the PTCDA/CuPc interface can effectively dissociate the photogenerated excitons into holes and electrons and prevent them from recombining [23] and (ii) there is intermolecular hydrogen bonding between PTCDA and CuPc, and consequently the overlap between the HOMO of CuPc and the LUMO of PTCDA becomes significant. Thus, via process (1) holes and electrons can be efficiently generated in the HOMO of CuPc and in the LUMO of PTCDA, respectively, in PTCDA:CuPc composites. Note that the static inducement effect decreases rapidly with increasing NPB spacer thickness and almost vanishes when the NPB spacer thickness is greater than or equal to about 20 nm, as shown in Fig. 7(a). The working

mechanism of the ITO/PTCDA:CuPc anode is described as follows: when the ITO is biased positive, holes confined at the ITO/PTCDA:CuPc interface may effectively polarize PTCDA:CuPc pairs, efficiently generating holes in CuPc and electrons in PTCDA, and then holes are transferred into the NPB layer by CuPc aggregates and electrons into the ITO by PTCDA aggregates, thus generating a very efficient hole current. The static-inducement for very efficient hole-electron pair generation in PTCDA:CuPc is the reason why the ITO/PTCDA:CuPc anode structure is superior to the ITO/CuPc anode structure. For the ITO/ PTCDA:CuPc anode structure, if the thickness of the PTCDA: CuPc composite (such as 5 nm) is smaller than the optimal thickness of 10–20 nm, the number of PTCDA:CuPc pairs involved in hole-electron pair generation is smaller, hence generating less efficient hole current and resulting in reduced device performance. If the thickness of the PTCDA:CuPc composite is larger (e.g. 30 nm) than the optimal thickness of 10–20 nm, there is no more enhancement of hole-electron pairs generation, but the absorption of PTCDA:CuPc composite over Alq3 emission becomes remarkable, causing the degradation in device performance.

3.1.3. The significance and future development of the donor/ acceptor interface in OLEDs

Very recently, the planar and mixed donor/acceptor interfaces have also been used as very efficient interconnecting structures for tandem OLEDs [27], showing the versatility of the donor/acceptor pairs. However, it should be noted that all the donors and acceptors currently used to form the hole-generating interfaces in OLEDs exhibit significant absorption in the visible-light range, thus reducing the light out-coupling from the devices. Therefore, it is of great importance to develop wide-bandgap donors and acceptors. In addition, in order to increase the amplitude of hole current at the donor/acceptor interfaces, it is of much necessity to narrow down the offset between the HOMO of donor and LUMO of acceptor.

3.2. Increasing electron current in IBOLEDs via the combination of two n-doped layers

The n-doped organic electron acceptors, e.g., n-NTCDA, n-PTCDA, n-C_{60}, possess markedly higher conductivities but markedly lower capabilities of injecting electrons into electron transport layer (such as BCP, Alq3, etc.), as compared to the frequently used n-doped materials (such as n-BCP, n-Alq3, etc.) in OLEDs. However, recent work [13-16] shows that the combination of the above two classes of n-doped materals may increase current in IBOLEDs as described below.

3.2.1. Inverted OLEDs incorporated with the combination of Li_2CO_3:PTCDA and Li_2CO_3:BCP

Here first we will describe the optical and structural properties of n-doped materials and then the prperties of OLEDs fabricated from these materials.

3.2.1.1. Optical and structural properties of Li_2CO_3:PTCDA and Li_2CO_3:BCP

The optical properties of 1:2 Li_2CO_3:PTCDA and 1:4 Li_2CO_3:BCP are studied here and presented in Fig. 8. As seen in Fig. 8(a), compared to the intrinsic PTCDA, Li_2CO_3:PTCDA exhibits much lower intermolecular optical absorption at 558 nm [26], indicating severe distortion of the ordered π-π stack of PTCDA molecules caused by the doping with Li_2CO_3. In addition, a new sub-gap absorption centered at a wavelength of 686 nm appears, indicating the formation of the charge transfer state between the matrix and dopant in Li_2CO_3:PTCDA composite [28]. Fig. 8(b) shows that the edge of the optical absorption for 1:4 Li_2CO_3:BCP was slightly blue-shifted relative to that of intrinsic BCP, which implies the occurrence of electron transfer from the O^{2-} bonded to Li to BCP 1:4 Li_2CO_3:BCP composite [29].

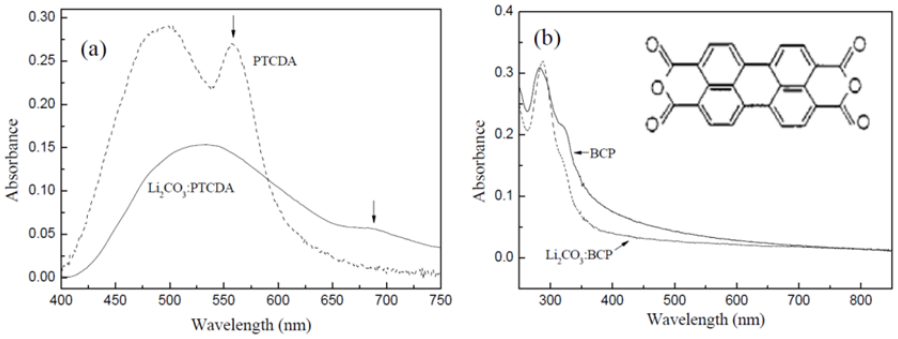

Figure 8. UV-vis absorption spectra for the 20 nm PTCDA and 1:2 Li_2CO_3:PTCDA thin films (a), and the 20 nm BCP and 1:2 Li_2CO_3:PTCDA thin films (b). The inset in (b) is the molecular structure of PTCDA.

3.2.1.2. Electrical properties of Li_2CO_3:PTCDA and Li_2CO_3:BCP

For studying the electrical properties we have fabricated the following two devices:
Device 6: ITO (anode)/ 1:4 Li_2CO_3:BCP 10 nm/ 1:2 Li_2CO_3:PTCDA 5 nm/ Alq3 65 nm/ Al (cathode);
Device 7: ITO (anode)/ 1:4 Li_2CO_3:BCP 5 nm/ 1:2 Li_2CO_3:PTCDA 10 nm/ Alq3 65 nm/ Al (cathode).

In device 6 with the structure of ITO (anode)/1:4 Li_2CO_3:BCP x nm/1:2 Li_2CO_3:PTCDA 15-x nm/Alq3 65 nm/Al (cathode), the electron current passes through Alq3 to 1:2 Li_2CO_3:PTCDA and to 1:4 Li_2CO_3:BCP connected in series. Therefore, the relative conductivity of 1:2 Li_2CO_3:PTCDA to 1:4 Li_2CO_3:BCP can be detected by observing the influence of 1:4 Li_2CO_3:BCP thickness on the device current. Fig. 9 exhibits that the current of device 6 is much lower than that of device 7 at a given driving voltage, demonstrating that 1:2 Li_2CO_3:PTCDA is much more conductive than 1:4 Li_2CO_3:BCP. This can be due to the following two factors: firstly, the charge carriers are more efficiently generated in 1:2 Li_2CO_3:PTCDA than in 1:4 Li_2CO_3:BCP due to the lower LUMO level of PTCDA than that of BCP. Secondly, the electron mobility of intrinsic PTCDA (3×10^{-6} $cm^2 \cdot V^{-1} \cdot s^{-1}$) is much higher

than that of BCP (6×10^{-7} $cm^2 \cdot V^{-1} \cdot s^{-1}$). Therefore, it might be feasible to improve the performance of IBOLED via the introduction of the Li_2CO_3:PTCDA composite onto the ITO cathode for enhancing current conduction.

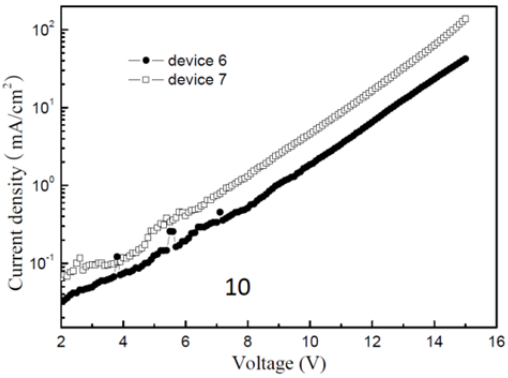

Figure 9. I-V characteristics for devices 6 and 7. As there is no Alq3 emission observed from the two devices in the measurement range, the current in both the two devices is considered to be comprised of electrons only.

3.2.1.3. Inverted OLED using the combination of Li_2CO_3:PTCDA and Li_2CO_3:BCP

We have fabricated the following three inverted devices and studied their characteristics.
Device 8: ITO (cathode)/ 1:2 Li_2CO_3:PTCDA 5 nm/ 1:4 Li_2CO_3:BCP 5 nm/ Alq3 40 nm/ NPB 40 nm/ MoO_3 10 nm/Al (anode);
Device 9: ITO (cathode)/ 1:4 Li_2CO_3:BCP 10 nm/ Alq3 40 nm/ NPB 40 nm/ MoO_3 10 nm/Al (anode);
Device 10: ITO (cathode)/ 1:2 Li_2CO_3:PTCDA 5 nm/ BCP 5 nm/ Alq3 40 nm/ NPB 40 nm/ MoO_3 10 nm/Al (anode).

Fig.10 shows the performance of devices 8 and 9. It can be seen in Fig. 10(a) that the driving voltage of device 8 for achieving a given current was reduced than that of device 9. To generate a current density of 100 mA/cm^2, device 8 needs a driving voltage of 7.1 V, smaller than that needed by device 9 (8.3 V). Device 8 also gives higher luminance than device 9 as shown in Fig. 10(b). At a driving voltage of 8 V, the luminance of device 8 is 6983 cd/m^2, in contrast to that of 1354 cd/m^2 for device 9. Fig. 10(c) shows that the current efficiency of device 8 is slightly lower than that of device 9, mostly because 1:2 Li_2CO_3:PTCDA exhibits some absorption over Alq3 emission, while 1:4 Li_2CO_3:BCP is nearly transparent in the visible-light range. Nevertheless, due to the marked reduction of driving voltage, device 8 provides higher power efficiency than device 9. It can be concluded that the two-layer combination of 1:2 Li_2CO_3:PTCDA and 1:4 Li_2CO_3:BCP outperforms the single 1:4 Li_2CO_3:BCP with regard to promoting the current conduction for the IBOLED.

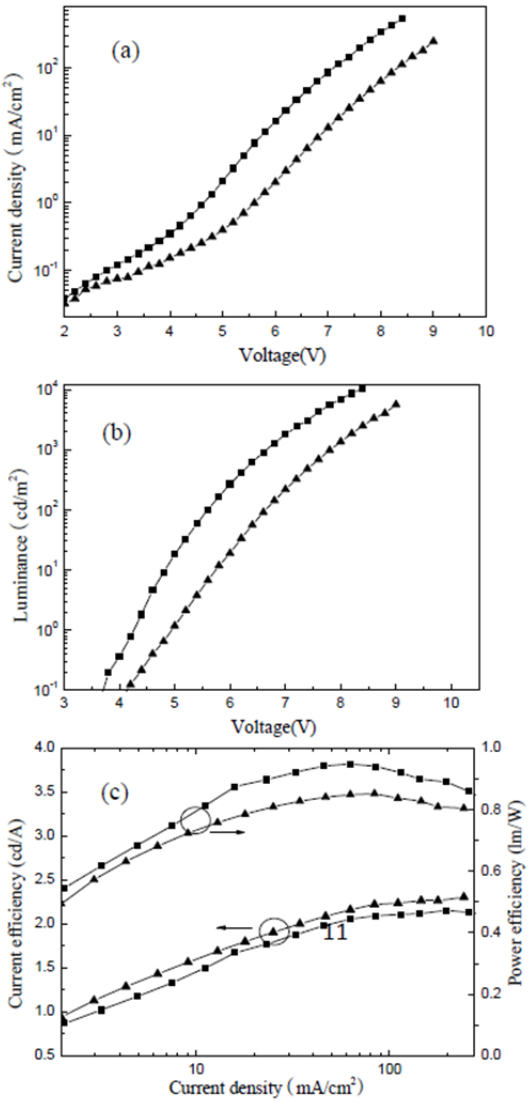

Figure 10. (a) I-V characteristics, (b) L-V characteristics, (c) current and power efficiencies versus current density of devices 8 (filled squares) and 9 (filled triangles). Both the devices give nearly the same Alq3 emission.

Figs. 10 (a) and (b) show that device 8 performs better that device 9, which may be attributed to the enhanced electron current due to the following : (i) In device 8, the electron injection is realized not only via tunneling, but also via thermionic emission due to relatively smaller energy barrier from ITO into the LUMO of PTCDA. (ii) The conductivity of 1:2 Li_2CO_3:PTCDA is higher than that of 1:4 Li_2CO_3:BCP, leading to reduced ohmic loss of

current conduction. Fig. 10(c) shows that the current efficiency of device 8 is slightly lower than that of device 9, mostly because 1:2 Li2CO3:PTCDA exhibits some absorption over Alq3 emission, while 1:4 Li2CO3:BCP is nearly transparent in the visible-light range. Nevertheless, due to the marked reduction of driving voltage, device 8 provides higher power efficiency than device 9. In terms of device 8, the issue of the efficient electron transfer from 1:2 Li_2CO_3:PTCDA into 1:4 Li_2CO_3:BCP needs to be addressed, since the LUMO level (4.6 eV) of PTCDA is 1.6 eV lower than that (3.0 eV) of BCP. In quest of the mechanism of electron transport over such a big Schottky barrier, device 10 is fabricated and characterized. As seen in Fig. 11, device 10 shows poor current-voltage and luminance-voltage characteristics. At a driving voltage of 10 V, it exhibits a current of 2.3 mA/cm^2 and a luminance of 4.1 cd/m^2, in clear contrary to 531 mA/cm^2 and 10492 cd/m^2 achieved at a driving voltage of 8.4 V in device 8. This greatly improved performance of device 8 relative to device 10 implies that the energy barrier for electron injection from PTCDA into BCP can be significantly reduced by fulfilling the double-sided n-doping to the Schottky interface.

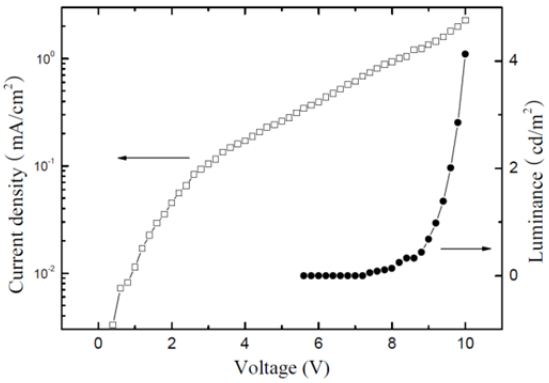

Figure 11. The I-V and L-V characteristics for device 10.

3.2.1.4. The working mechanism of the combination of Li_2CO_3:PTCDA and Li_2CO_3:BCP

The electronic structures of the interfaces of 1:2 Li_2CO_3:PTCDA/BCP and 1:2 Li_2CO_3:PTCDA/1:4 Li_2CO_3:BCP are schematically shown in Fig. 5. The LUMO-LUMO offset at organic heterojunction can be varied by the interfacial dipole Δ given by [30]:

$$\Delta = \left(1 - \frac{1}{2}\left(\frac{1}{\varepsilon_1} + \frac{1}{\varepsilon_2}\right)\right)(CNL_1 - CNL_2)_{initial}, \quad (2)$$

where ε_1 and ε_2 are the low frequency dielectric constants for the two organic materials, CNL_1 and CNL_2 represent their charge neutrality levels. In the case of 1:2 Li_2CO_3:PTCDA/BCP heterojunction, considering that the dielectric constant of n-doped PTCDA is larger compared to that of the undoped PTCDA (1.9) and taking ε_{BCP}~1.4, $(1/\varepsilon_1+1/\varepsilon_2)$ is estimated to be ~0.7. Provided that the CNL for n-doped PTCDA is roughly equal to that of undoped PTCDA(-4.8 eV) due to the Fermi level pinning [22] and CNL of BCP~-3.8 eV, Eq. (2) yields an interface

dipole Δ_1=-0.65 eV, resulting a 0.65 eV downwards shift of the vacuum level (VL) on the BCP side LUMO as shown in Fig. 12(i). Thus, the electron injection barrier from the LUMO of 1:2 Li_2CO_3:PTCDA to hat of BCP reduces roughly to 0.95 eV. This shows that the electron transport through the 1:2 Li_2CO_3:PTCDA/BCP interface can be small in device 10. For the 1:2 Li_2CO_3:PTCDA/1:4 Li_2CO_3:BCP heterojunction, the term $(1/\varepsilon_1+1/\varepsilon_2)$ is assumed to be ~0.2, because the low-frequency dielectric constants of the doped materials are larger compared to the undoped materials. Provided the CNL for n-doped PTCDA~-4.8 eV and the CNL for n-doped BCP~3.2 eV [31], Eq. (2) yields an interface dipole Δ_2= -1.44 eV, leading to a 1.44 eV downwards shift of the vacuum level (VL) in the doped BCP side, as shown in Fig. 12(ii). Accordingly, the electron injection barrier at the 1:2 Li_2CO_3:PTCDA/1:4 Li_2CO_3:BCP heterojunction is estimated to be 0.16 eV, suggesting that the double n-doping can induce significant realignment of molecular levels of organic-organic heterojunction. Thus, the contact becomes ohmic, resulting in efficient electron current and increasing device performance (the case of device 8).

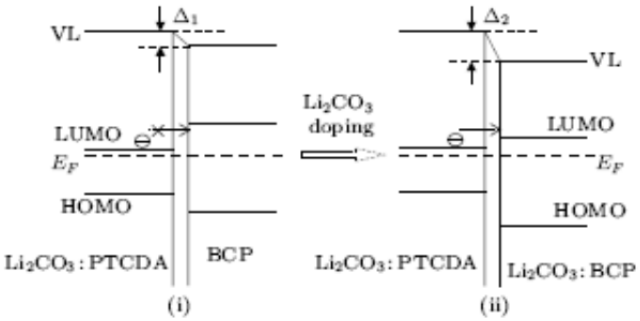

Figure 12. Schematic diagram for depicting the electronic structures of the interfaces of 1:2 Li_2CO_3:PTCDA/BCP (i) and 1:2 Li_2CO_3:PTCDA/1:4 Li_2CO_3:BCP (ii), both deposited onto the ITO substrates. For simplicity, the gap states are not shown. The E_F, HOMO, and horizontal dotted arrow represent the Fermi level, highest occupied molecular orbital, and the electron-injecting process, respectively.

3.2.2. Inverted OLEDs incorporating the combination of MoO_3 and Li_2CO_3:BCP

There has been some controversy about the intrinsic property of MoO_3, which has been intensively investigated in OLEDs for improving the hole injection. It is considered by some groups that MoO_3 should act as a hole conductor with highest occupied molecular orbital (HOMO) and lowest unoccupied molecular orbital (LUMO) levels of ~5.4 eV and ~2.3 eV, respectively [32]. Recently, however, it is suggested [33] that due to being doped by oxygen vacancy defects MoO_3 intrinsically offers n-typed conduction with deep-lying HOMO and LUMO levels of ~9.7 eV and ~6.7 eV, respectively. The enhanced hole injection by the MoO_3 intervention may be attributed to the process that one electron in the HOMO level of organic hole-transporting material can be easily transferred into the LUMO level of MoO_3 because the Fermi level of MoO_3 is necessarily pinned close to the HOMO level of p-typed organic conductor [33]. Here, we investigate MoO_3 as electron injection layer in IBOLEDs and show

that MoO_3 in association with an n-doped layer of BCP can enable the efficient electron injection.

3.2.2.1. Conductivity of MoO_3 and Li_2CO_3:BCP

For comparing the conductivity due to the incorporation of MoO_3 and Li_2CO_3:BCP in OLEDs, We have fabricated the following two devices:

Device 11: ITO (cathode)/ MoO_3 10 nm/ 1:4 Li_2CO_3:BCP 5 nm/ Alq3 80 nm/ Al (anode);
Device 12: ITO (cathode)/ MoO_3 5 nm/ 1:4 Li_2CO_3:BCP 10 nm/ Alq3 80 nm/ Al (anode).

The conductivity of an organic thin film can be measured via a vertical sandwiched structure. However, the diffusion of the top metal electrode into organic thin film enables the chemical reaction between metal atoms and organic molecules, leading to the unavoidable alteration for the intrinsic property of organic thin film. Thus, devices 11, 12 are fabricated to qualitatively compare the conductivities of MoO_3 and 1:4 Li_2CO_3:BCP. In the electron-only device with structure of ITO (cathode)/ MoO_3 x nm/ 1:4 Li_2CO_3:BCP 15-x nm/ Alq3 80 nm/ Al (anode), the electrons are firstly injected into MoO_3, then transported through MoO_3, 1:4 Li_2CO_3:BCP, and Alq3 in sequence, and finally transfered into Al. Thus, the study of the I-V characteristics with the varying thickness of MoO_3 can be studied from devices 11 and 12 as shown in Fig. 13. As seen in Fig. 13, the current density of device 11 is greater than that of device 12 in the whole applied voltage range. This clearly indicates that MoO_3 (10 nm thick) is more conducting than 1:4 Li_2CO_3:BCP (10 nm thick) composite. Thus, MoO_3 can be expected to act as a better electron transport layer in the IBOLED

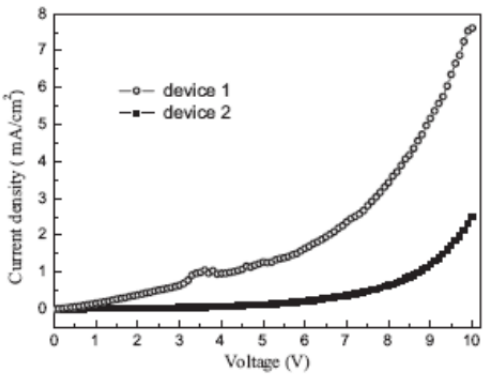

Figure 13. The I-V characteristics of devices 11 (open circles) and 12 (fill squares). No Alq3 electroluminescence is detected in the measurement range for these two devices.

3.2.2.2. Inverted OLEDs using the combination of MoO_3 and Li_2CO_3:BCP

We have fabricated and studied the characteristics of the following IBOLEDs:
Device 13: ITO/ MoO_3 5 nm/ 1:4 Li_2CO_3:BCP 5 nm/ Alq3 40 nm/ NPB 60 nm/ MoO_3 10 nm/Al;
Device 14: ITO/ 1:4 Li_2CO_3:BCP 10 nm/ Alq3 40 nm/ NPB 60 nm/ MoO_3 10 nm/Al;
Device 15: ITO/ MoO_3 5 nm/ BCP 5 nm/ Alq3 40 nm/ NPB 60 nm/ MoO_3 10 nm/Al;

Device 16: ITO/ MoO_3 5 nm/ 1:4 Li_2CO_3:BCP 5 nm/ Alq3 50 nm/ NPB 60 nm/ MoO_3 10 nm/Al;
Device 17: ITO/ MoO_3 5 nm/ 1:4 Li_2CO_3:BCP 5 nm/ Alq3 60 nm/ NPB 60 nm/ MoO_3 10 nm/Al;
Device 18: ITO/ MoO_3 5 nm/ 1:4 Li_2CO_3:BCP 5 nm/ Alq3 70 nm/ NPB 60 nm/ MoO_3 10 nm/Al;

Fig. 14 shows the performances of devices 13 and 14. Device 13 shows nearly the same I-V characteristics as device 14, but the luminance and current efficiency of device 13 are higher than those of device 14. At a luminance of 100 cd/m^2, device 13 achieves a driving voltage of 7.51 V and a current efficiency of 1.39 cd/A, in comparison with 7.72 V and 1.08 cd/A, respectively, reached in device 14. At a luminance of 1000 cd/m^2, device 13 exhibits a driving voltage of 8.86 V and a current efficiency of 2.0 cd/A, in comparison with 9.04 V and 1.62 cd/A obtained in device 14. The improved performance of device 13 over device 14 may be attributed to the reduced dopant diffusion from Li_2CO_3:BCP into Alq3 as a result of the thinner Li_2CO_3:BCP in device 13.

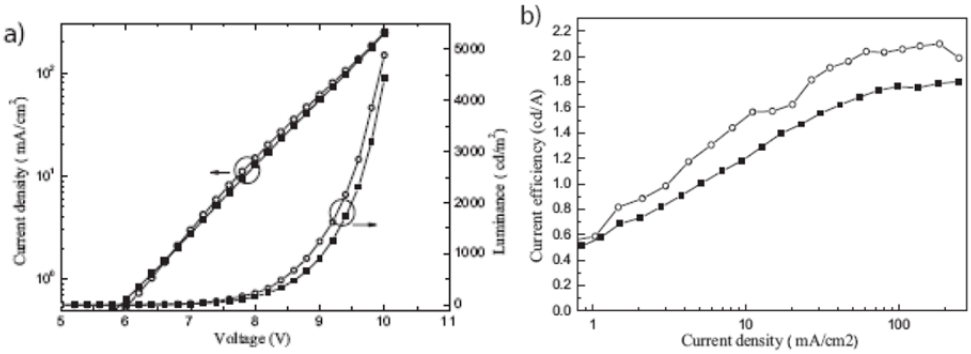

Figure 14. (a) I-V and L-V characteristics and (b) current efficiency versus current density characteristics for devices 13 (circles) and 14 (squares).

3.2.2.3. Mechanism of operation in the combination of MoO_3 and Li_2CO_3:BCP

Despite that MoO_3 exhibits better electron conduction than 1:4 Li_2CO_3:BCP composite, device 13 produces nearly the identical electron current as device 14, demonstrating that there must be some voltage drop across the MoO_3/1:4 Li_2CO_3:BCP interface in device 13. In an effort to investigate the mechanism of the electron transfer from MoO_3 to 1:4 Li_2CO_3:BCP, the characteristics of device 15 is studied as presented in Fig. 15, which shows that device 15 exhibits poor I-V characteristics with no Alq3 electroluminescence observed, suggesting there is a big Schottky barrier for electron injection from MoO_3 to BCP. The marked performance difference between devices 13 and 15 indicates that the LUMO-LUMO offset at the MoO_3/BCP interface can be remarkably lowered due to doping Li_2CO_3 into BCP, which can be explained by the interfacial dipole calculated by Eq. (2). In the case of the MoO_3/BCP heterojunction, taking ε_{MoO3}~20 and ε_{BCP}~1.4 [30], the item of $(1/\varepsilon_1+1/\varepsilon_2)$ is estimated to be ~0.76. Considering that the CNL (work function) of MoO_3 is -6.9 eV [33] and that of BCP~-3.8 eV, Eq. (2) yields an interface dipole Δ_1=-1.92 eV. This results in a 1.92 eV downward shift of the vacuum level on the BCP side. Thus, the Schottky barrier for the electron injection from the LUMO of MoO_3 to

that of BCP is roughly 1.78 eV, determining that the electron transport through the MoO_3/BCP interface is very inefficient in the case of device 15. For the MoO_3/1:4 Li_2CO_3:BCP heterojunction, the item of $(1/\varepsilon_1+1/\varepsilon_2)$ is assumed to be ~0.1, because the low-frequency dielectric constant of the doped BCP is larger compared to the undoped one [30]. Provided that the CNL of MoO_3~-6.9 eV and that of n-doped BCP~-3.2 eV [20], Eq. (2) yields an interface dipole Δ_2=-3.52 eV, leading to a 3.52 eV downwards shift of the vacuum level on the doped BCP side. Thus, the electron injection barrier at the MoO_3/1:4 Li_2CO_3:BCP heterojunction is estimated to be roughly 0.18 eV, favoring the efficient electron injection in MoO_3 and hence better device performance (the case of device 13). In addition, the intrinsic Schottky barrier for electron injection from Li_2CO_3:BCP to Alq3 is estimated to be ~0.4 eV according to Eq. (2).

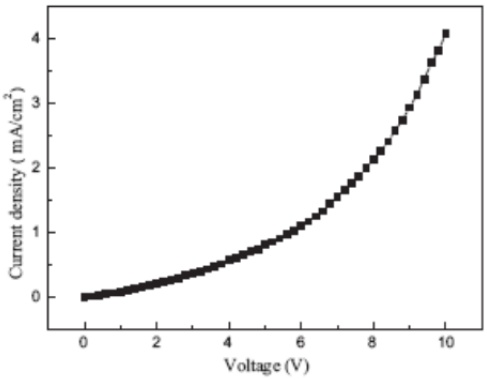

Figure 15. The I-V characteristics of device 15. There was no Aq3 electroluminescence detected in the measurement range, suggesting that the electron current was very inefficient in device 15.

3.2.2.4. The dopant diffusion in the Li_2CO_3:BCP

Fig. 16(a) shows the I-V characteristics of devices 13, 16, 17 and18 and Fig. 16(b) presents the plot of the voltage drop as a function of the thickness of Alq_3 film. The inset of Fig. 16(a) displays the luminance properties of these devices. Fig. 16(b) indicates that the driving voltage across the device varies linearly with the Alq3 thickness when the device current (I) increases from 2 to 100 mA/cm^2. Thus, the average internal electric field in the Alq3 layer ($F_{av, Alq3}$) of device 13 is calculated [34, 35] as shown in Fig. 17. It can be seen in Fig. 17 that $F_{av, Alq3}$ increases monotonously as I increases from 2 to 30 mA/cm^2, and becomes gradually saturated when I > 30 mA/cm^2. The turning point at I = 30 mA/cm^2 of the $F_{av, Alq3}$ versus I characteristics can be due to the efficient diffusion of Li_2CO_3 from Li_2CO_3:BCP into Alq3, which can not only lead to some exciton-quenching effect in the emissive layer, coincident with the observations in Fig. 14(b), but also it can leave the emissive layer n-doped, thereby reducing the interfacial energy barrier [13] and making Alq3 more conductive. Also seen in Fig. 17 is that when I varies between 2 and 30 mA/cm^2, the total device current versus the average electric field in Alq3 appears to follow a Richardson–Schottky (RS) behavior, $I \propto \exp[\beta\cdot(F_{av,Alq3})^{1/2}]$, due to the good linear fit (R^2=0.997) to the log I versus $F^{1/2}_{av, Alq3}$ plot. Accordingly, the coefficient β is

calculated to be 28.1 $(MV/cm)^{-1/2}$, approximately one and half times larger than the value of β_{RS}=11.6 $(MV/cm)^{-1/2}$, implied by the RS formula of $\beta_{RS} = (e^3/4\pi\varepsilon_0\varepsilon_r)^{1/2}/k_BT$ (taking ε_r ~1.6). This discrepancy is consistent with the other reported observations [34]. It should be stressed here that the electric field at the Li_2CO_3:BCP/Alq3 interface, responsible for electron injection, may be different to the average electric field in the Alq3 layer. Interestingly, when I exceeds 30 mA/cm^2, the total device current versus the average electric field in Alq3 diverts from the RS behavior due to the deteriorated linear fit (R^2=0.989) to the log I versus $F^{1/2}_{av,\ Alq3}$ plot. This diversion is likely to be attributed to the fact that the conclusive electron injection process shifts from the Li_2CO_3:BCP/Alq3 interface to the MoO_3/1:4 Li_2CO_3:BCP heterojunction as a result of the efficient Li_2CO_3 diffusion towards the anode in device 13.

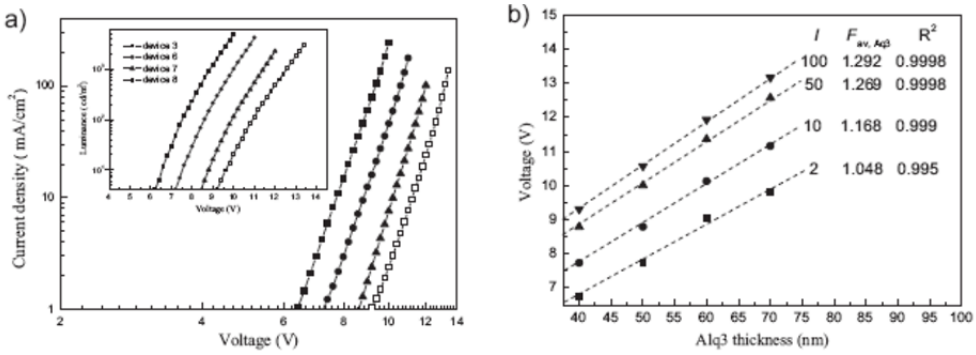

Figure 16. (a) The I-V characteristics of devices 13 (solid squares), 16 (solid circles), 17 (solid triangles), and 18 (open squares). (b) The total voltage drop across device versus the Alq3 thickness at various current densities (I in mA/cm^2). The dashed lines represent the linear fits to the plots, and their slopes denote the the average internal electric fields in the Alq3 layer ($F_{av, Alq3}$ in MV/cm). R^2 represents the linear-fit correlation coefficient. The inset (a) shows the L-V characteristics for devices 13, 16, 17 and 18.

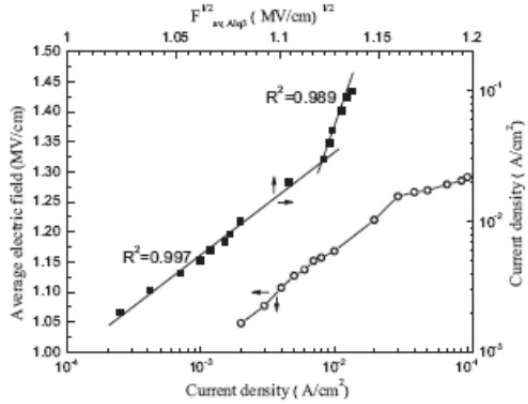

Figure 17. The average internal electric fields in the Alq3 layer (circles, bottom X + left Y) and the dependence of of the total current density on the average internal electric field (squares, top X + right Y) in device 13. The two straight lines with correlation coefficients (R^2) mean the linear fits.

3.2.3. The inverted OLEDs incorporating the combination of n-NTCDA and Li_2CO_3:BCP

To maximize the performance for the combination of two n-ETLs, the n-ETL contacting the cathode needs to meet the two requirements: high conductivity and good transparency over the visible light range. Thus, the n-NTCDA was chosen to function with Li_2CO_3:BCP.

3.2.3.1. The properties of the NTCDA deposited onto the ITO

NTCDA is a class of n-type organic semiconductor with a LUMO level at 4.0 eV [36]. It can have the electronic interactions with the active metals like In or Mg at room temperature, which is attributed to the partial charge transfer from the metal to carbonyl oxygen of NTCDA [37]. It is also reported that NTCDA shows strong electronic interaction with metal atoms in an ITO substrate to form charge transfer (CT) complexes or gap states [38]. The formation of a CT complex can not only lower the energy barrier for hole injection from ITO into N,N'-bis-(1-naphthl)-diphenyl-1,1'-biphenyl-4,4'-diamine, but also can offer a conducting path to assist hole transport [38]. Thus, the introduction of NTCDA onto the ITO anode can significantly improve the hole current and thereby the performance of regular OLED. Nevertheless, it needs to be stressed that the electronic interaction between active metal and NTCDA can leave NTCDA n-doped via the spontaneous charge transfer from metal atom to NTCDA [37].

The four NTCDA thin films have been fabricated and characterized in Fig. 18. Fig. 18(a) shows that the NTCDA thin films both deposited on ITO and glass are crystalline, proven by their same diffraction peaks at $2\theta=11.8^{o}$. Fig. 18(b) shows the UV-VIS absorption spectra of the four NTCDA thin films. All the NTCDA thin films gave two peaks at the wavelengths of 368 nm and 390 nm assigned to π-π^{*}. Compared with the 15 nm NTCDA thin film on glass, the 15 nm NTCDA thin film on ITO shows a broad absorption peak from 420 nm to 600 nm, which becomes weaker with the decreasing thickness of the NTCDA on ITO [39]. The emergence of a new sub-gap absorption indicates the formation of the CT complex between NTCDA and ITO as a result of the upward diffusion of In atoms from ITO into NTCDA and the concomitant interaction between In and anhydride groups of NTCDA. Thus, the NTCDA thin films on the ITO are conclusively crystalline and n-doped. The conductivity of the n-doped NTCDA (n-NTCDA) is reported to be as high as 9.29×10^{-4} S/cm [4], almost two orders of magnitude higher than that of n-BCP [31]. Hence, according to the concept of using two n-ETLs mentioned above, the NTCDA on the ITO may be applied as the first n-ETL to enhance the electron conduction in IBOLEDs.

3.2.3.2. The comparison between the electron injection structures of ITO/ BCP:Li_2CO_3 (4:1) 10 nm and ITO/NTCDA 3 nm/ BCP:Li_2CO_3 (4:1) 7 nm

For this study we fabricated the following IBOLEDs:
Device 19. ITO/ BCP:Li_2CO_3 (4:1) 10 nm/ Alq3 40 nm/ CBP 60 nm/ MoO_3 10 nm/Al;
Device 20. ITO/NTCDA 3 nm/ BCP:Li_2CO_3 (4:1) 7 nm /Alq3 40nm/CBP 60 nm/ MoO_3 10 nm/Al;
Device 21. ITO/NTCDA 3 nm/ BCP 7 nm /Alq3 40nm/ CBP 60 nm/ MoO_3 10 nm/Al;

Device 22. ITO/NTCDA 5 nm/ BCP:Li_2CO_3 (4:1) 5 nm /Alq3 40nm/ CBP 60 nm/ MoO_3 10 nm/Al;
Device 23. ITO/NTCDA 7 nm/ BCP:Li_2CO_3 (4:1) 3 nm /Alq3 40nm/ CBP 60 nm/ MoO_3 10 nm/Al.

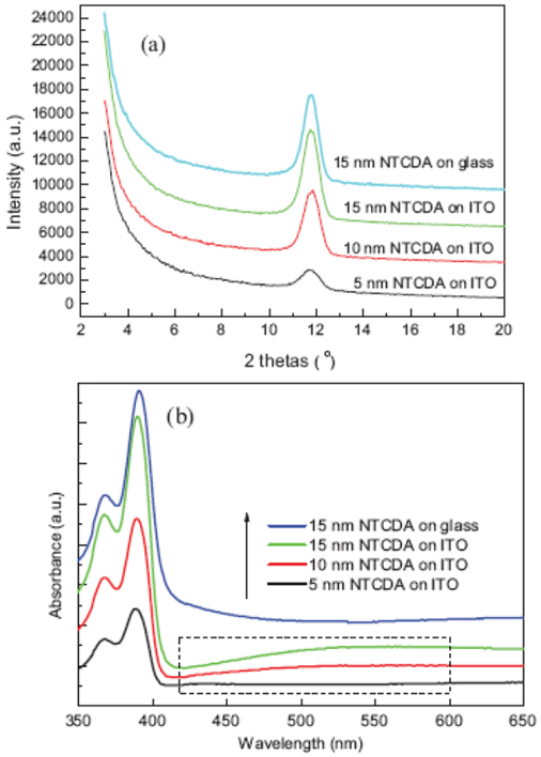

Figure 18. The XRD (a) and UV-Vis absorption spectra (b) of the 5, 10, 15 nm NTCDA thin films on the ITO and the 15 nm NTCDA thin film on the glass. Due to the limitation of the instrument, we were unable to detect the sub-gap absorption in the 5 nm NTCDA on the ITO. Note that, the 3 nm NTCDA thin film on the ITO is also confirmed to be crystalline.

Fig. 19(a) shows the I-V characteristics of devices 19 and 20. As expected, device 20 showed higher current density than device 19 at a given voltage between 3 and 10 V. To generate a current density of 100 mA/cm^2, device 20 needed a driving voltage of 8.0 V, smaller than that for device 19 (9.0 V). Fig. 19(b) shows device 20 also exhibits enhanced luminance than device 19. At a driving voltage of 10 V, the luminance of device 20 is found to be 11706 cd/m^2, in comparison with 4016 cd/m^2 for device 19. Fig. 19(c) shows that the maximum current efficiency in device 20 is 2.29 cd/A, 38% higher than that of 1.66 cd/A in device 19, mostly attributed to the following two factors: firstly, the intervention of the NTCDA improved the hole-electron balance in device 20 relative to device 19; secondly, the NTCDA was nearly transparent in the visible-light range. Hence, it may be concluded that the

combination of n-NTCDA and 1:4 Li_2CO_3:BCP excels the single 1:4 Li_2CO_3:BCP in promoting the current conduction and efficiency of the IBOLED.

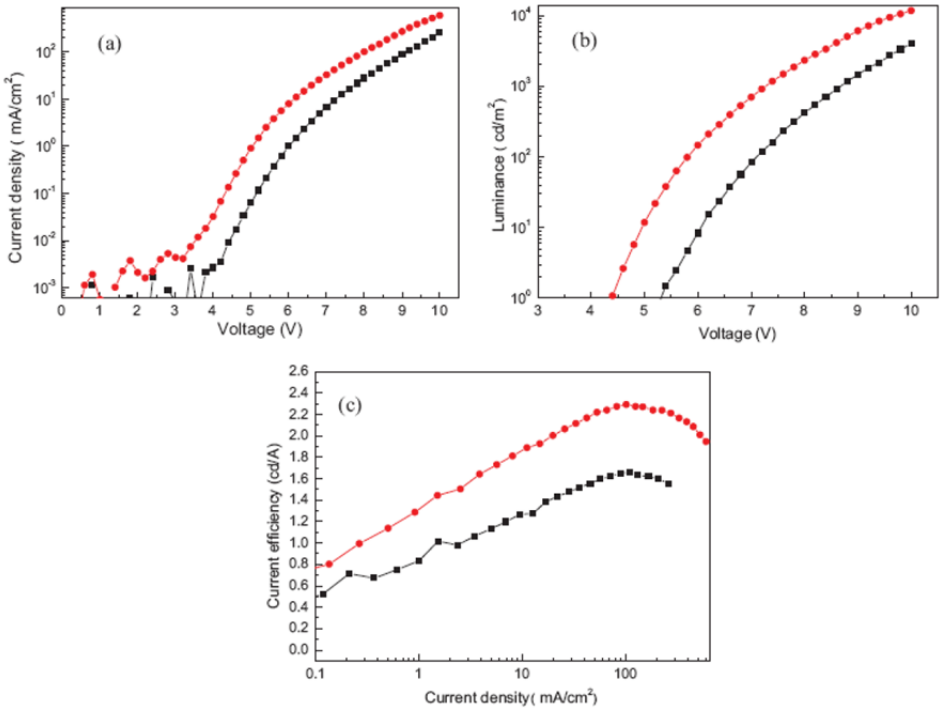

Figure 19. The I-V (a), luminance versus voltage (b), current efficiency versus current density (c) characteristics for devices 19 (squares) and 20 (circles).

3.2.3.3. The mechanism of electron transport from n-NTCDA into BCP:Li_2CO_3 (4:1)

In device 20, how the electrons are efficiently transported from n-NTCDA into 1:4 Li_2CO_3:BCP needs to be addressed, since the LUMO level (4.0 eV) of NTCDA is 1.0 eV lower than that (3.0 eV) of BCP. In quest of the relevant mechanism, device 21 is fabricated and its characteristics are shown in Fig. 20. As seen in Fig. 20, device 21 exhibits poor current--voltage characteristics. At a driving voltage of 10 V, it yields a current of 3.63 mA/cm^2 and no light emission, which is clearly contrary to 601 mA/cm^2 and 11709 cd/m^2 achieved in device 20. The greatly improved performance of device 20 relative to device 21 indicates that the energy barrier for electron injection from n-NTCDA into BCP is significantly reduced by fulfilling the n-doping on the BCP side [13].

The electronic structures of the interfaces of n-NTCDA/BCP and n-NTCDA/1:4 Li_2CO_3:BCP are schematically shown in Fig. 21. The LUMO-LUMO offset at the organic heterojunction can be varied by the interfacial dipole (Δ) expressed as Eq. (2). In the case of n-NTCDA/BCP heterojunction, considering the dielectric constant of n-NTCDA is large

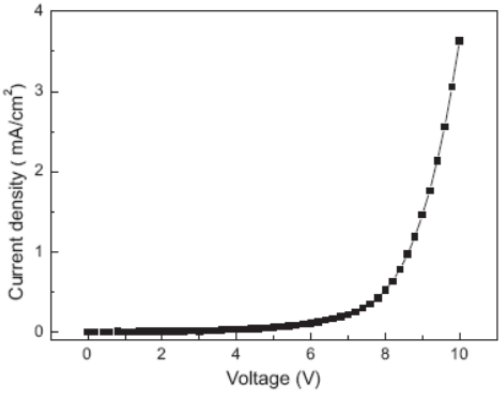

Figure 20. The I-V characteristics of device 21. Note that, there was no Alq3 emission observed in the measurement range.

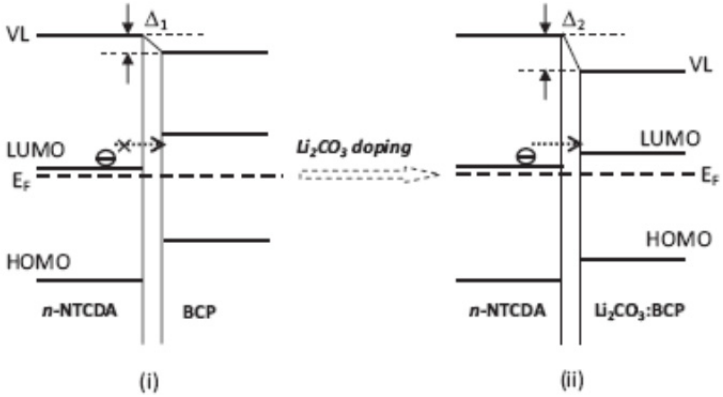

Figure 21. Schematic diagrams for depicting the electronic structures at the interfaces of n-NTCDA/BCP (i) and n-NTCDA/1:4 Li_2CO_3:BCP (ii), both deposited onto the ITO substrates. For simplicity, the gap states are not shown. The E_F, HOMO, and horizontal dotted arrow represent the Fermi level, highest occupied molecular orbital, and the electron-injecting process, respectively.

compared to that (1.6) of the undoped NTCDA and taking ε_{BCP}~1.4, $(1/\varepsilon_1+1/\varepsilon_2)$ is estimated to be ~0.7. Provided that the CNL for n-NTCDA is roughly -4.2 eV due to the Fermi level pinning [22] and taking the CNL of BCP~-3.8 eV, Eq. (2) yields an interface dipole Δ_1=-0.26 eV, which results in a 0.26 eV downward shift of the vacuum level (VL) on the BCP side as seen in Fig. 21(i). Thus, the energy barrier from the LUMO of n-NTCDA to that of BCP is estimated to be about 0.74 eV, determining that the electron transport through the n-NTCDA/BCP interface is very poor in the case of device 22. For the n-NTCDA/1:4 Li_2CO_3:BCP heterojunction, $(1/\varepsilon_1+1/\varepsilon_2)$ is assumed to be ~0.2, because the low-frequency dielectric constants of the doped materials are larger compared to the undoped materials. Provided that the CNL for n-NTCDA ~-4.2 eV and the CNL for n-BCP~-3.2 eV, Eq. (2) yields

an interface dipole Δ_2=-0.90 eV, leading to a 0.90 eV downward shift of the VL in the n-BCP side, as as shown in Fig. 21(ii). The electron injection barrier from n-NTCDA to 1:4 Li_2CO_3:BCP is estimated to be roughly 0.10 eV. Thus, the interface becomes ohmic, enabling the efficient electron conduction and hence enhaced device performance (the case of device 20).

3.2.3.4. The effect of the NTCDA thickness on the current conduction of IBOLED

It is found that the device performance is strongly influenced by the thickness of the NTCDA on ITO as a hole injection layer [39]. Therefore, the dependence of the IBOLED performance on the NTCDA on ITO as n-ETL has been investigated and the observed characteristics are shown in Fig. 22 for devices 20, 22, and 23. It can be seen that the current density of the IBOLED using the 3 nm NTCDA is found to be higher than that of the IBOLEDs using the 5 and 7 nm NTCDA at a given voltage between 3 and 10 V. It may be explained as follows. When the thickness of the NTCDA exceeds 3 nm, the formation of the CT complex near the NTCDA top surface starts to vanish [38], that is, the surface density of the CT complex near NTCDA top surface starts to decrease, leading to a reduced generation of free electrons therein. Thus, the electron conduction across the whole NTCDA thin film decreases and gives rise to the decreased IBOLED current.

3.2.4. The tandem OLEDs incorporating the combination of Li_2CO_3:PTCDA and Li_2CO_3:BCP

Tandem OLEDs consisting of two light emitting units stacked vertically in series have been demonstrated [40, 41]. Compared to the single light emitting unit, the two-unit tandem OLED can provide the prolonged working lifetime and higher luminance but nearly the same power efficiency, because the driving voltage of the tandem OLED is twice that of the single light emitting unit at a given current density. Therefore, the tandem OLEDs have been widely recognized as a promising technology for organic flat-panel displays and solid-state lighting sources in the market competition. The future development of the tandem OLEDs is to further reduce their high driving voltage via both the structure optimization of the single light emitting unit and the improvement of the interconnecting structure.

It has been recognized that the voltage drop across the interconnected structure is the key to determining the operation voltage of the tandem OLEDs [40]. In order to minimize the series resistance of the interconnected structure, it is of great necessity to reduce the ohmic loss of the current conduction in this structure provided that the energy losses due to the internal charge generation and injections have already been optimized. Thus, it is meaningful to seek for a higher-conductivity alternative to the conventional n-doped organic electron transporters. Recently, the n-doped PTCDA has been used to reduce the driving voltage of OLEDs due to its higher conductance than the conventional n-doped organic electron conductors (BCP and Alq3) [13, 42], implying that the n-doped PTCDA may act as a potential candidate for the n-type section to reduce the current loss in the tandem structure.

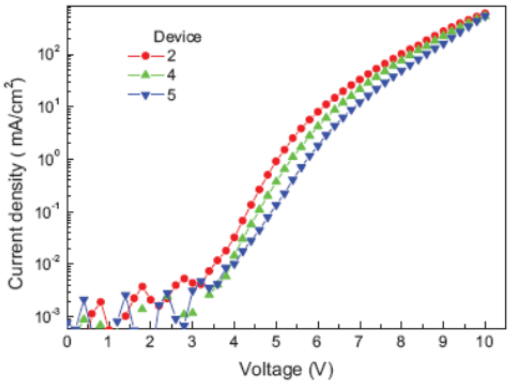

Figure 22. The I-V characteristics of devices 20 (circles), 22 (uptriangles), and 23 (downtriangles).

Here, a 5 nm lithium carbonate doped PTCDA (1:2 Li_2CO_3:PTCDA) has been incorporated in the n-type section of the interconnected structure. Compared to the tandem OLED of 5 nm Li_2CO_3 doped BCP (1:4 Li_2CO_3:BCP)/ MoO_3, the tandem OLED of 5 nm 1:2 Li_2CO_3:PTCDA/ 5 nm MoO_3 showed the enhanced electrical and luminous performance, due to the higher electron conductivity of 1:2 Li_2CO_3:PTCDA than that of 1:4 Li_2CO_3:BCP. The working mechanism of the improved interconnecting structure is also discussed.

3.2.4.1. The optical properties of the IS1 and IS2

Fig. 23 shows the optical transmittance of two interconnected structures. It can be seen that the 5 nm 1:2 Li_2CO_3:PTCDA/ 5 nm MoO3 (IS1) is nearly transparent in the visible-light range, but the 5 nm 1:4 Li_2CO_3:BCP/ 5 nm MoO3 (IS2) shows slight light absorption from 400 to 700 nm, due to the narrow optical band gap of PTCDA (1.7 eV).

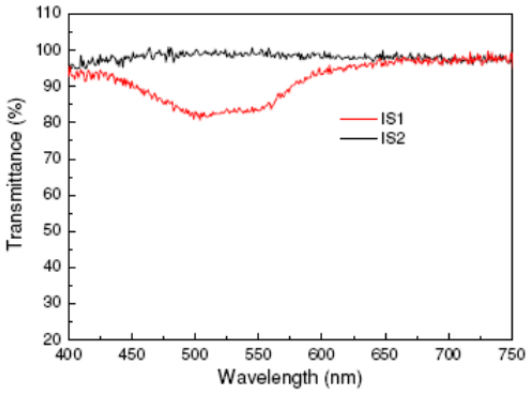

Figure 23. The optical properties of the IS1 and IS2 deposited on the quartz glasses.

3.2.4.2. The electrical properties of the IS1 and IS2

For studying the electrical properties, we have fabricated the following two devices:
Device 24: ITO (anode)/ 1:2 Li_2CO_3:PTCDA 5 nm/ MoO_3 5 nm/ NPB 80 nm/ Al (cathode).
Device 25: ITO (anode)/ 1:4 Li_2CO_3:BCP 5 nm/ MoO_3 5 nm/ NPB 80 nm/ Al (cathode).

The I-V characteristics of devices 24 and 25 are shown in Fig. 24. Because the ITO anode is unable to inject holes into n-doped PTCDA and BCP, and the Al cathode provides very inefficient electron injection into NPB, the current versus voltage plots of devices 24 and 25 mostly represent the internal charge generation and transport in the devices IS1 and IS2. Because devices 24 and 25 have the same interfaces of 5 nm MoO_3 and 80 nm NPB, the internal charge generation and hole conduction for the two devices are identical. Therefore, the difference between the I-V characteristics of devices 24 and 25 exhibit mostly the electron conduction through the IS1 and IS2. The current density of device 24 shown in Fig. 24 is found to be greater than that of device 25, indicating the resistance of IS1 is less than that of the IS2. Hence, the IS1 tandem structure is advantageousthan IS2 because IS1 results in less ohmic loss of electron conduction than IS2.

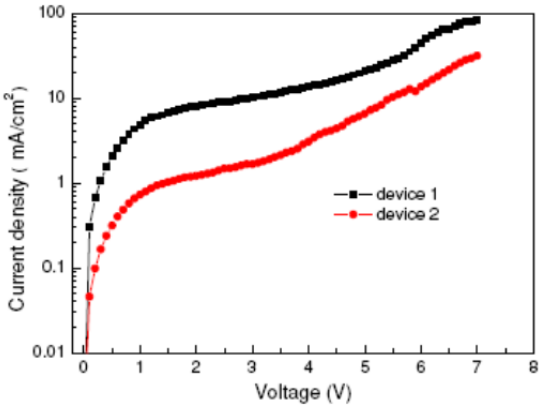

Figure 24. The I-V characteristics of devices 24 (blak curve) and 25 (red curve).

The LUMO-LUMO offset at the 1:2 Li_2CO_3:PTCDA/MoO_3 interface can be estimated via calculating the interfacial dipole through Eq. (2). The term $(1/\varepsilon_1+1/\varepsilon_2)$ is assumed to be ~0.1, taking ε_1~20 and ε_2~20 because the low-frequency dielectric constant of the doped PTCDA is larger compared to the undoped one. Provided that the CNL for n-doped PTCDA~-4.8 eV [30] and the CNL for MoO_3~-6.9 eV, Eq. (2) yields an interface dipole Δ=2.0 eV, leading to a 2.0 eV upward shift of the vacuum level on the MoO_3 side. Thus, the electron injection barrier at the 1:2 Li_2CO_3:PTCDA/MoO_3 heterojunction is estimated to be roughly 0.1 eV, favoring the very efficient electron injection from MoO_3 into 1:2 Li_2CO_3:PTCDA. Likewise, the electron transport barrier from MoO3 to 1:4 Li_2CO_3:BCP is estimated to be 0.18 eV [14], meaning that the electron current can flow from MoO3 into 1:4 Li_2CO_3:BCP very efficiently as well. As a result, the increased electron transport in the IS1 over IS2 may be mostly attributed to the higher electron conductivity of 1:2 Li_2CO_3:PTCDA than 1:4 Li_2CO_3:BCP [13].

3.2.4.3. The performance comparison between the S, T1, and T2 devices

A single OLED S with structure of ITO/ NPB 80 nm/ Alq3 55 nm/ 1:4 Li_2CO_3:BCP 5 nm/ Al and two tandem OLEDs, T1 and T2, have been fabricated for this study as shown in Fig. 25.

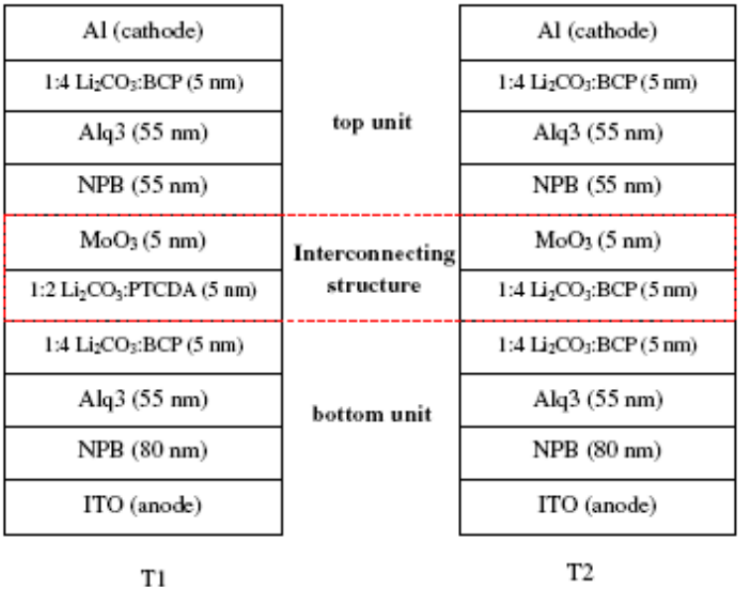

Figure 25. The schematic diagrams for the structures of the T1 and T2 device.

Fig. 26 shows the electroluminescent spectra of S, T1, and T2 devices. It is obvious that these three devices produce nearly the same Alq3 emission peaking at a wavelength of about 520 nm, demonstrating that IS1 and IS2 behave as good optical spacers without bringing any appreciable microcavity effect.

The electrical and luminous properties of the three devices are shown in Fig. 27. As expected, the T1 device gives higher current density than T2 device, which may be mostly attributed to the more efficient current conduction in IS1 than in IS2. Accordingly, the device T1 is also brighter than the device T2. At a driving voltage of 19 V, the luminance of T1 is 3656.8 cd/m^2, brighterr than 2323.9 cd/m^2 of T2 device. Because of some absorption in IS1 over the Alq3 emission, the T1 device shows slightly less current efficiency than T2 device when the current density ranges from 0.1 to 80 mA/cm^2. The maximum current efficiency of T2 device (4.86 cd/A) is found to be almost twice that of S device (2.51 cd/A). However, due to the reduced working voltage required for T1 than for T2, these two tandem OLEDs show comparable power efficiencies when the current density ranges from 0.1 to 80 mA/cm^2. Both of them have the maximum power efficiency of about 0.84 lm/W, slightly greater than that of the single-unit device S (0.80 lm/W). Note that, compared to both T1 and T2 devices, S device gives much lower power efficiency at a current density ≤ 10 mA/cm^2 and slightly increased power efficiency at current density ≥ 45 mA/cm^2.

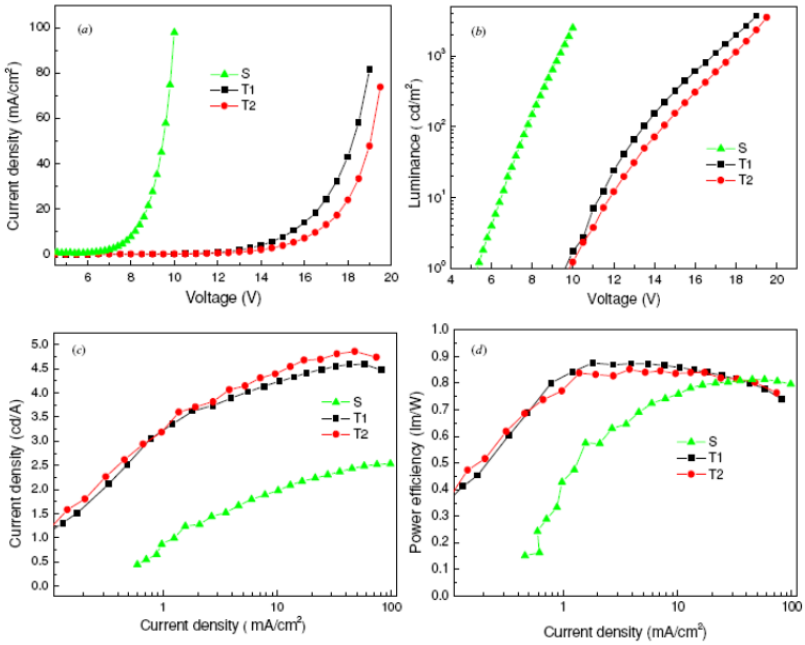

Figure 26. The I-V (a), luminance versus voltage (b), current efficiency versus current density (c), and power efficiency versus current density (d) characteristics of the S, T1, and T2 devices.

In Table I are listed the performance data of S device at a driving voltage of 9 V and those of T1 and T2 devices at a driving voltage of 18 V. The current density of T2 device at 18 V is lower than that of the S device at 9 V, while the luminance and current efficiency of the T2 device are nearly twice of those of the S device, and the power efficiencies of the T2 and S devices were nearly same. This indicates that the IS2 can effectively connect the two units in T2 device but with a marked voltage drop across it. The current density of T1 device at 18 V is 50% higher than that of S device at 9 V, its luminance is about three times that of S device, its current efficiency is twice that of S device, and its power efficiency is equal to that of S device. The current density of T1 device at 18 V is more than that of S device at 9 V. This may be attributed to the following two factors. Firstly, the voltage drop across IS1 is markedly lower compared to IS2 and secondly, the NPB layer in the upper unit is of much less thickness than that in the bottom unit.

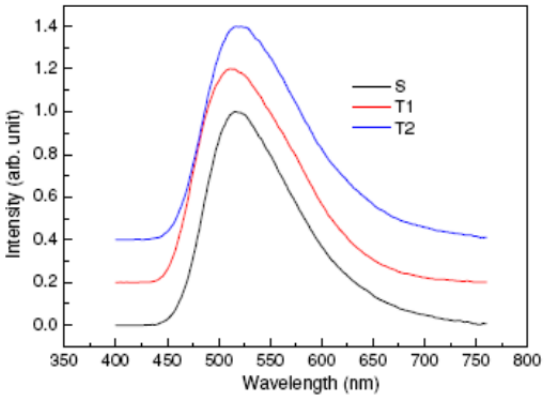

Figure 27. The electroluminescent spectra of the S, T1, and T2 devices.

Device	S	T1	T2
Voltage (V)	9	18	18
I (mA/cm2)	27.7	43.1	23.4
L (cd/m2)	637.6	1974.1	1124.8
CF (cd/A)	2.3	4.59	4.69
PF (lm/W)	0.80	0.80	0.82

Table 1. The performance data of the devices S, T1, and T2 . I, L, CF, and PF represent current density, luminance, current efficiency, and power efficiency, respectively.

It should be pointed out that, due to the poor ability of Li_2CO_3:PTCDA to inject electrons into the traditional electron transport materials (e.g., Alq3, BCP), an n-doped layer with high-lying LUMO level, n-doped BCP must be involved to facilitate the electron injection from n-doped PTCDA into the traditional electron transport materials [13]. Thus, IS1 cannot only reduce the ohmic loss of current conduction, but also can offer comparable electron injection into the bottom unit, relative to IS2.

3.2.5. The design concept of uniting two n-doped layers and its significance in OLEDs

The n-doped organic electron acceptors, e.g., n-NTCDA, n-PTCDA and n-C_{60}, possess markedly higher conductivities but lower capabilities of injecting electrons into electron transport layer (such as BCP, Alq3, etc.), as compared to the frequently used n-doped materials (such as n-BCP, n-Alq3, etc.) in organic light emitting diodes (OLEDs). In this section, we study the combination of the above two classes of n-doped materals, called the structure of uniting double n-doped layers (n-ETL_1/ n-ETL_2/ ETL). The characteristics for the structure of n-ETL_1/ n-ETL_2/ ETL are as follows: n-ETL_1 features the LUMO level greater than 4.0 eV (i.e., the LUMO level lies below 4.0 eV) and possesses higher conductivity of transporting electrons; n-ETL2 features the LUMO level less than 3.4 eV (i.e., the LUMO level lies above 3.4 eV) and possesses better capability of injecting into ETL; at the n-ETL_1/ n-ETL_2 interface, due to the quasi Fermi level alignment. In this caes, the energy barrier for the electron injection from n-ETL_1 to n-ETL_2 is usually less than 0.2 eV. Such a constructed combination cannot only significantly reduce ohmic loss in electron conduction, but also possess strong capability of injecting electrons into ETL. It has been demonstrated that the structure of uniting double n-doped layers enables remarkable enhancement in both electron current and luminous performance for inverted and tandem OLEDs. Therefore, it can be considered as an advanced electron injection technology, which can significantly push forward the commercializations of organic flat-panel displays and solid-state lighting.

4. Conclusions

Currently, the commerical application of organic lighting is being held back by the fact that the power efficiency of OLEDs drops drastically with the increase in active area.This means that the luminous flux of OLEDs does not increase automatically if the emissive area is increased. Thus, it becomes the top priority to develop the charge injection techniques which can increase the power and emittance of OLEDs. The charge injection techniques discussed in this chapter are still in their very early stages, and their further development depends mostly by inventing new materials which can meet all the requirements listed above.

Author details

Dashan Qin
Institute of Polymer Science and Engineering, School of Chemical Engineering, Hebei University of Technology, Tianjin, People's Republic of China

Jidong Zhang
State Key Laboratory of Polymer Physics and Chemistry, Changchun Institute of Applied Chemistry, Chinese Academy of Sciences, Changchun, Jilin Province, People's Republic of China

Acknowledgement

The authors are grateful for the financial supports from the National Science Foundation of China (Grant No 50803014) and from Open research fund of state key laboratory of polymer physics and chemistry, Changchun Institute of Applied Chemistry, Chinese Academy of Sciences.

5. References

[1] C.W. Tang and S. A. Vanslyke, Organic electroluminescent diodes. Appl. Phys. Lett. 51: 913 (1987).

[2] S. Braun, W. Osikowicz, Y. Wang and W. R. Salaneck W R, Energy level alignment regimes at hybrid organic-organic and inorganic-organic interfaces. Org. Electron. 8: 14 (2007).

[3] S. Braun S, W. R. Salaneck and M. Fahlman, Energy-level alignment at organic/metal and organic/organic interfaces. Adv. Mater. 21: 1450 (2009).

[4] K. Walzer K, B. Maennig, M. Pfeiffer and K. Leo,Highly Efficient Organic Devices Based on. Electrically Doped Transport Layers. Chem.Rev. 107: 1233 (2007).

[5] G. H. Cao, D. S. Qin, J. S. Cao, M. Guan, Y. P. Zeng and J. M. Li, Organic light emitting diodes with an organic acceptor/donor interface involved in hole injection. Chin. Phys. Lett. 24: 1380 (2007).

[6] G. H. Cao, D. S. Qin, J. S. Cao, M. Guan, Y. P. Zeng and J. M. Li, Improved performance in organic light emitting diodes with a mixed electron donor-acceptor film involved in hole injection. J. Appl. Phys. 101: 124507 (2007).

[7] Y. Y. Yuan, S. Han, D. Grozea and Z. H. Lu, Fullerene-organic nanocomposite: a flexible material platform for organic light-emitting diodes. Appl. Phys. Lett. 88: 093503 (2006).

[8] X. Zhou, M. Pfeiffer, J. S. Huang, J. Blochwitz-Nimoth, D. S. Qin, A. Werner, J. Drechesel, B. Maennig and K. Leo, Low-voltage inverted transparent vacuum deposited organic light-emittingdiodes using electrical doping. Appl. Phys. Lett. 81: 922 (2002).

[9] T. Y. Chu, J. F. Chen, S. Y. Chen, C. H. Chen, Comparative study of single and multiemissive layers in inverted white organic light-emitting devices. Appl. Phys. Lett. 89: 113502 (2006).

[10] N. J. Watkins, L. Yan and Y. Gao, Electronic structure symmetry of interfaces between pentacene and metals. Appl. Phys. Lett. 80: 4384 (2002).

[11] W. Song, S. K. So, J. Moulder, Y. Qiu, Y. Zhu and L. Cao, Study on the interaction between Ag and tris(8-hydroxyquinoline) aluminum using x-ray photoelectron spectroscopy. Surf. Interface Anal. 32: 70 (2001).
[12] M. Thomschke, S. Hofmann, S. Olthof, M. Anderson, H. Kleemann, M. Schober, B. Lüssem and K. Leo, Appl. Phys. Lett. 98: 083304 (2011).
[13] C. R. Cheng, Y. H. Chen, D. S. Qin, W. Quan and J. S. Liu, Inverted bottom-emission organic light emitting diode using two n-doped layers for the enhanced performance. Chin. Phys. Lett. 27: 117801 (2010).
[14] D. S. Qin, J. S. Liu, Y. H. Chen, C. R. Cheng and W. Quan, Inverted bottom-emission organic light emitting diodes using MoO_3 for both hole and electron injections. Phys. Solidi Status A 208: 1976 (2011).
[15] D. S. Qin, L. Chen, Y. H. Chen, J. S. Liu, G. F. Li, W. Quan, J. D. Zhang and D. H. Yan, Enhanced performance in inverted organic light emitting diode assisted by an interlayer of crystalline and n-doped 1,4,5,8-naphthalene-tetracarboxylic-dianhydride, Phys. Solidi Status A 209: 790 (2012).
[16] J. S. Liu, Y. H. Chen, D. S. Qin, C. R. Cheng, W. Quan, L. Chen and G. F. Li, Improved interconnecting structure for a tandem organic light emitting diode. Semicond. Sci. Technol. 26: 095011 (2011).
[17] C. W. Tang, Two-layer organic photovoltaic cell. Appl. Phys. Lett. 48: 183 (1986).
[18] C. Rost, S. Karg, W. Riess, M. A. Loi, M. Murgia and M, Muccini, Ambipolar light-emitting organic field-effect transistor. Appl. Phys. Lett. 85: 1613 (2004).
[19] J. Wang, H. B. Wang, J. X. Yan, H. C. Huang and D. H. Yan, Organic heterojunction and its application for double channel field-effect transistors. Appl. Phys. Lett. 87: 093507 (2005).
[20] L. Chkoda, C. Heske, M. Sokolowski and E. Umbach, Improved band alignment for hole injection by an interfacial layer in organic light emitting devices. Appl. Phys. Lett. 77: 1093 (2000).
[21] P. E. Burrows and S. R. Forrest, Electroluminescence from trap-limited current transport in vacuum deposited organic light emitting devices, Appl. Phys. Lett. 64: 2285 (1994).
[22] I. G. Hill, A. Rgjagopal, A. Kahn and Y. Hu, Molecular level alignment at organic semiconductor-metal interfaces. Appl. Phys. Lett. 73: 662 (1998).
[23] S. R. Forrest, W. Y. Yoon, L. Y, Leu and F. F. So, Optical and electrical properties of isotype crystalline molecular organic heterojunctions. J. Appl. Phys. 66: 5908 (1998).
[24] B. P. Rand, J. Xue, S. Uchida and S. R, Forrest, Mixed donor-acceptor molecular heterojunctions for photovoltaic applications. I. Material properties. J. Appl. Phys. 98: 124902 (2005).
[25] P. Liu, Q. Li, M. S. Huang and W. Z. Pan, High open circuit voltage organic photovoltaic cells based on oligothiophene derivatives. Appl. Phys. Lett. 89: 213501 (2006).

[26] V. Bulović, P. E. Burrows, S. R. Forrest, J. A. Cronin and M. E. Thompson, Study of localized and extended excitons in 3,4,9,10-perylenetetracarboxylic dianhydride (PTCDA) I. Spectroscopic properties of thin films and solutions. Chem. Phys. 210: 1 (1996).

[27] Y. H. Chen, J. S. Chen, D. G. Ma, D. H. Yan and L. X. Wang, Effect of organic bulk heterojunction as charge generation layer on the performance of tandem organic light-emitting diodes. J. Appl. Phys. 110: 074504 (2011).

[28] D. R. T. Zahn, G. N. Gavrila and G. Salvan, Electronic and Vibrational Spectroscopies Applied to Organic/Inorganic Interfaces. Chem. Rev. 107: 1161 (2007).

[29] Y. Yuan, D. Grozea, S. Han and Z. H. Lu, Interaction between organic semiconductors and LiF dopant. Appl. Phys. Lett. 85: 4959 (2004).

[30] A. Kahn, W. Zhao, W. Y. Gao, H. Vazquez and F. Flores, Doping-induced realignment of molecular levels at organic–organic Heterojunctions. Chem. Phys. 325: 129 (2006).

[31] G. Parthasarathy, C. Shen, A. Kahn and S. R. Forrest, Lithium doping of semiconducting organic charge transport materials. J. Appl. Phys. 89: 4986 (2001).

[32] C. Tao, S. P. Ruan, X. D. Zhang, G. H. Xie, L. Shen, X. Z. Kong, W. Dong, C. X. Liu and W. Y. Chen, Performance improvement of inverted polymer solar cells with different top electrodes by introducing a MoO_3 buffer layer. Appl. Phys. Lett. 93: 193307 (2008).

[33] M. Kröger, S. Hamwi, J. Meyer, T. Riedl, W. Kowalsky and A, Kahn, Role of the deep-lying electronic states of MoO_3 in the enhancement of hole-injection in organic thin films. Appl. Phys. Lett. 95: 123301 (2009).

[34] E. Tutiš, D. Berner and L. Zuppiroli, Internal electric field and charge distribution in multilayer organic light-emitting diodes. J. Appl. Phys. 93: 4594 (2003).

[35] S. W. Shi and D. G. Ma, Investigation on internal electric field distribution of organic light-emitting diodes (OLEDs) with Eu_2O_3 buffer layer. Phys. Status Solidi A 206: 2641 (2009).

[36] Y. Shirota and H. Kageyama, Charge carrier transporting molecular materials and their applications in devices. Chem. Rev. 107: 953 (2007).

[37] H. Tachikawa, H. Kawabata, R. Miyamoto, K. Nakayama and M. Yokoyama, Experimental and Theoretical Studies on the Organic–Inorganic Hybrid Compound: Aluminum-NTCDA Co-Deposited Film. J. Phys. Chem. B 109: 3139 (2005).

[38] P. Jeon, H. Lee, J. Lee, K. Jeong, J. W. Lee and Y. Yi, Interface state and dipole assisted hole injection improvement with 1,4,5,8,-naphthalene-tetracarboxylic-dianhydride in organic light-emitting devices. Appl. Phys. Lett. 99: 073305 (2011).

[39] Y. M Koo and O. K. Song, Spontaneous charge transfer from indium tin oxide to organic molecules for effective hole injection. Appl. Phys. Lett. 94: 153302 (2009).

[40] L. S. Liao and K. P. Klubek, Power efficiency improvement in a tandem organic light-emitting diode. Appl. Phys. Lett. 92: 223311 (2008).

[41] C. W. Chen, Y. J. Lu, C. C. Wu, E. H. E. Wu, C. W. Chu and Y. Yang, Effective connecting architecture for tandem organic light-emitting devices. Appl. Phys. Lett. 87: 241121 (2005).

[42] C. R. Cheng, Y. H. Chen, D. S. Qin, W. Quan and J. S. Liu, Lithium carbonate doped 3, 4, 9, 10 perylenetetracarboxylic dianhydride for enhanced performance in organic light emitting diode Chin. J. Lumin. 32: 387 (2011).